metals

MDPI

Article

Hydrogen-Induced Cracking in CGHAZ of Welded X80 Steel under Tension Load

Jinxin Gou [1,2], Xiao Xing [1,2,*], Gan Cui [1,2], Zili Li [1,2,*], Jianguo Liu [1,2] and Xiangyuan Deng [1,2]

[1] College of Pipeline and Civil Engineering, China University of Petroleum (East China), Qingdao 266580, China
[2] Shandong Key Laboratory of Oil & Gas Storage and Transportation Safety, Qingdao 266580, China
* Correspondence: 20170079@upc.edu.cn (X.X.); zilimenhuzu@163.com (Z.L.)

Abstract: X80 steel is extensively used in hydrogen environments and is susceptible to hydrogen embrittlement (HE). This paper studied the hydrogen-induced cracking (HIC) behavior in the coarse-grained heat-affected zone (CGHAZ) of X80 steel welds, through applying in situ hydrogen-charging tensile experiments, hydrogen permeation experiments, and various surface analysis techniques. It is shown that a few hydrogen atoms can significantly decrease a material's elongation and reduction of area. When the heat input (HI) was 29.2 kJ/cm, the material had minor sensitivity to hydrogen embrittlement. The tensile fractures were ductile without hydrogen. However, the fracture surface exhibited brittle fracture with hydrogen. With increased HI, the HE fracture showed a transition of intergranular fracture→intergranular and transgranular mixed fracture→transgranular fracture. In the presence of hydrogen, the grain boundaries of elongated strips were prone to the formation of intergranular cracks under a tension load, and the hydrogen embrittlement resistance of the bulk lath bainite (LB) was weak. The hydrogen embrittlement susceptibility of pure granular bainite (GB) was lower. Fine LB and GB composite structures could remarkably inhibit intergranular cracks, giving the steel a superior resistance to hydrogen embrittlement.

Keywords: carbon steel; tensile; hydrogen diffusion; SEM; hydrogen embrittlement

check for updates

Citation: Gou, J.; Xing, X.; Cui, G.; Li, Z.; Liu, J.; Deng, X. Hydrogen-Induced Cracking in CGHAZ of Welded X80 Steel under Tension Load. *Metals* **2023**, *13*, 1325. https://doi.org/10.3390/met13071325

Academic Editor: Babak Shalchi Amirkhiz

Received: 7 June 2023
Revised: 23 June 2023
Accepted: 28 June 2023
Published: 24 July 2023

Copyright: © 2023 by the authors. Licensee MDPI, Basel, Switzerland. This article is an open access article distributed under the terms and conditions of the Creative Commons Attribution (CC BY) license (https://creativecommons.org/licenses/by/4.0/).

1. Introduction

The development of the hydrogen energy industry is a vital engine in optimizing the energy structure and promoting the transformation and upgrading of traditional industries [1–4]. Hydrogen storage and transportation is the bridge between hydrogen production and hydrogen energy applications [5,6]. China plans to build the first west-to-east hydrogen pipeline, with a total length of more than 400 km. In order to save transportation costs, X80 steel, suitable for large-diameter and high-pressure pipelines, will be widely used in hydrogen environments. In addition, the X80 steel pipelines currently in service are affected by cathodic overprotection and high-voltage transmission line interference, which causes hydrogen generation and penetration into the pipeline [7–10]. All these factors expose X80 steel to the risk of hydrogen embrittlement [11–13].

Whether exposed to high-pressure hydrogen or cathodic hydrogen evolution, once the hydrogen atoms are adsorbed on the metal surface and enter the pipeline [14], they accumulate in the hydrogen trap [15,16], which will cause hydrogen embrittlement (HE), especially in the weld area of a pipeline [17,18]. The multiplicity of grain orientations, grain boundaries, and dislocations caused by welding changes the mechanical properties of the material [19–22]. Pipe fracture failure due to insufficient toughness of the girth weld is one of the main failure modes of high-strength steel pipes. The welded joint's heat-affected zone (HAZ) [23–25] is a unique area between the weld and the base material (BM). Due to a non-uniformity of organization [26,27], it is easy to produce local defects and stress concentrations. This is the most vulnerable failure zone in the weld [28–30].

To date, the susceptibility of different metallographic structures of the X80 steel coarse-grained heat-affected zone (CGHAZ) to HE under tension load has not been fully characterized and understood. This knowledge is critical in helping to prevent hydrogen-induced cracking (HIC) in X80 steel hydrogen pipelines. This work investigated the HIC behavior in the CGHAZ of X80 steel welds using in situ hydrogen-charging tensile tests, hydrogen permeation experiments, and various surface analysis techniques. These results are expected to be used as the reference for the design and fabrication process of hydrogen pipelines.

2. Experimental

2.1. Materials and Specimens

Test specimens used in this work were taken from a sheet of X80 steel pipeline. The chemical composition of the steel contains (wt.%): C 0.07, Cu 0.221, Cr 0.266, Si 0.216, Mn 1.8, Ni 0.168, Mo 1.82, Nb 0.105, P 0.0137, Ti 0.013, Al 0.026, N 0.003, S 0.0009 and Fe balance.

The process of specimen machining is shown in Figure 1. First, slices of 16 × 180 × 2.2 mm^3 and 34 × 150 × 2.2 mm^3 were axially cut from X80 pipeline steel using wire cutting. Subsequently, the Gleeble 3500 thermal simulator (DSI, New York, NY, USA) was employed to conduct the heat treatment of the sheet [31]. The red part was the uniform temperature zone in the simulated welding heat treatment. Then, the heat-treated specimens were processed into tensile and hydrogen-permeable specimens with wire cutting. The surface of the specimen was ground with silicon carbide sandpaper to a grain size of 600, 800, and 1200, then polished with W5 diamond slurry. The specimen was then degreased with acetone and dehydrated with ethanol.

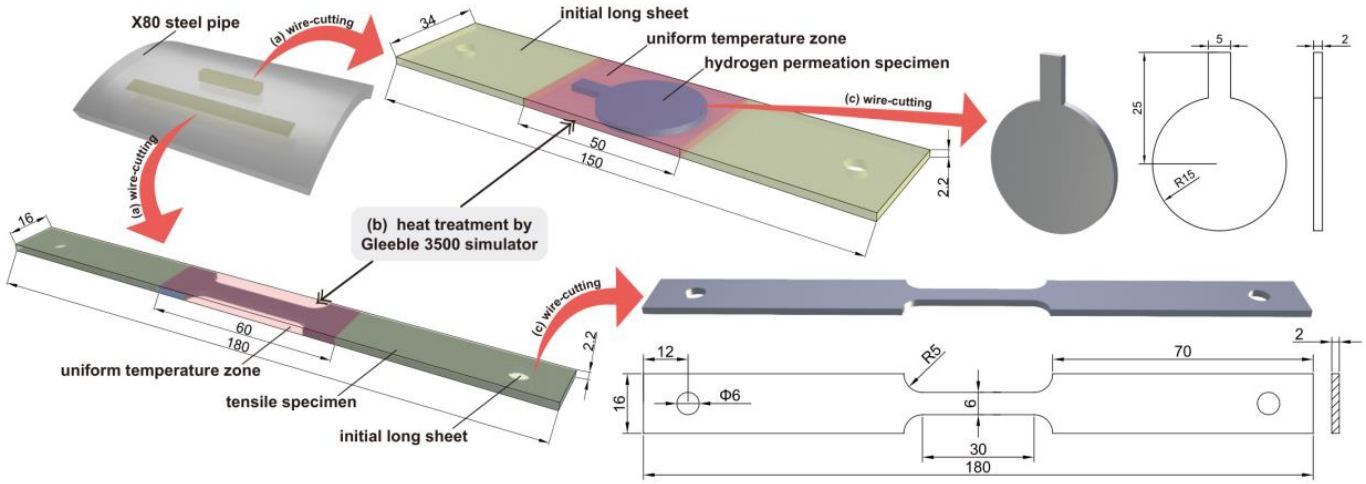


Figure 1. Schematic diagram illustrating the processes for specimen manufacturing and the specimen dimensions, adapted with permission from [32] (unit: mm).

Through a spiral submerged arc welding experiment of X80 steel, heat input curves were obtained from thermocouples pre-buried at different positions from the weld [29]. The cooling time from 800 °C to 500 °C ($t_{8/5}$) was obtained according to the heat input curve of CGHAZ [32,33]. The actual $t_{8/5}$ was 15.5s, and the corresponding welding heat input was 18.1 kJ/cm. We changed the cooling time $t_{8/5}$ and calculated the heat input corresponding to different cooling times, according to the theoretical and empirical formula of welding. The calculated thermal simulation parameters are shown in Table 1.

Table 1. CGHAZ thermal simulation parameters adapted from [34].

Label	Heating Rate (°C/s)	Peak Temperature (°C)	Holding Time (s)	Cooling Time $t_{8/5}$ (s)	Heat Input (kJ/cm)
HI08.5	150	1350	1	4.5	8.5
HI18.1				15.5	18.1
HI29.2				39.0	29.2
HI38.3				68.5	38.3
HI48.5				109.0	48.5

2.2. Metallographic Observation

The specimens were etched in a mixed solution of 4% nitric acid and ethanol and then observed with a ZEISS Axio Imager A2m (Carl Zeiss AG, Oberkochen, Germany) metallurgical microscope. The microstructures of CGHAZ under different heat inputs are shown in Figure 2. HI08.5 and HI18.1 were mainly composed of bulk lath bainite (LB), and LB was more finely interwoven in HI08.5. In HI29.2, LB was divided by granular bainite (GB), the composite structure was mainly composed of fine LB and GB. As the heat input continued to increase, the HI38.2 and HI48.5 were mainly composed of GB. With the increase in the heat input, the content of LB gradually decreased, while that of GB increased gradually [35].

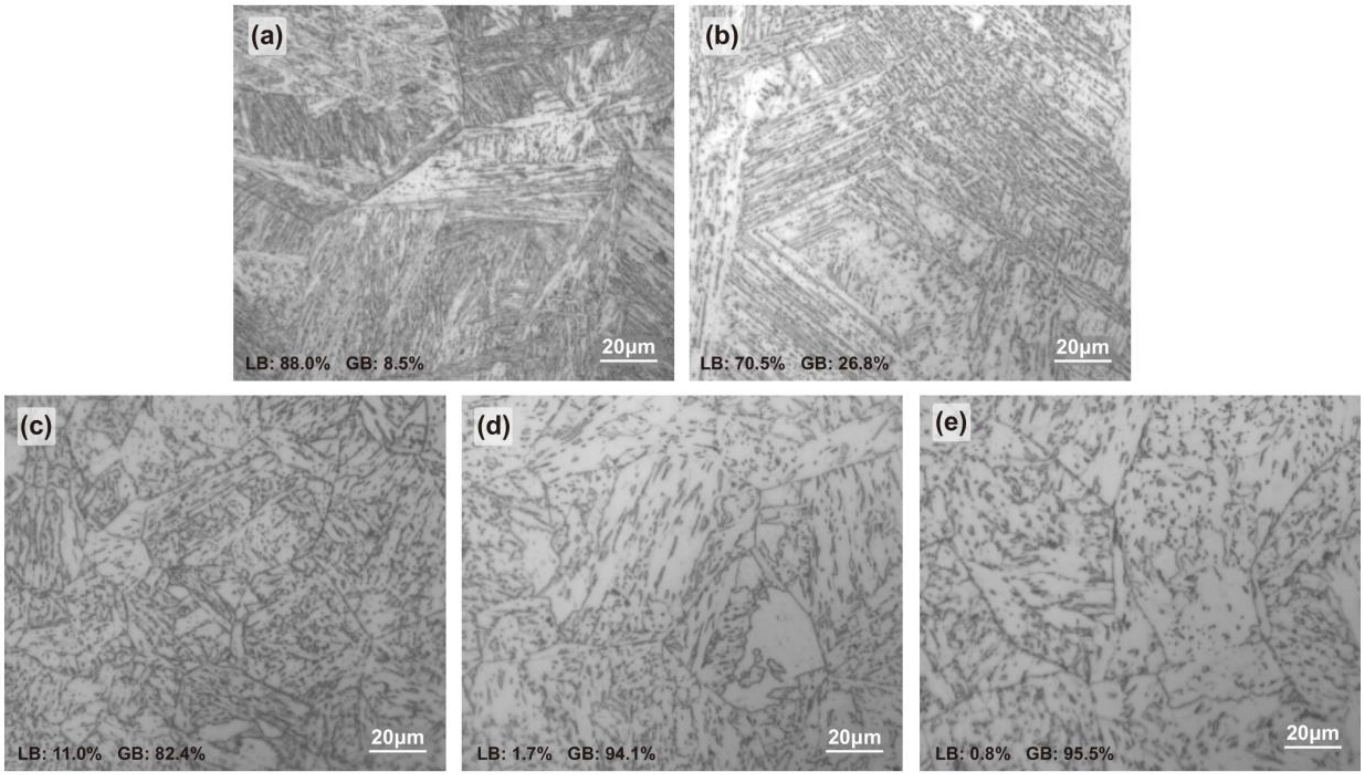


Figure 2. Metallographic structure of CGHAZ in welded X80 steel: (**a**) HI08.5, (**b**) HI18.1, (**c**) HI29.2, (**d**) HI38.3, and (**e**) HI48.5.

2.3. Tensile and Hydrogen Permeation Testing

The in situ hydrogen charging tensile device [34] is shown in Figure 3a. The type of tensile machine used in the tensile experiment in this paper was a slow strain stress testing machine WDML-50, which was manufactured by LETRY in 2020, and the in situ electrochemical hydrogen charging method was used to charge the specimen with hydrogen during the stretching process [36]. The electrochemical charging solution contained

0.5 mol/L H_2SO_4 + 0.2 g/L CH_4N_2S [37]. The hydrogen charging current densities were 5 mA/cm^2, 10 mA/cm^2, 20 mA/cm^2, 30 mA/cm^2, and 40 mA/cm^2; the hydrogen charging temperature was 20 °C; and the pre-charging time was 1.5 h. Stretching was performed at 20 °C, with a strain rate of 10^{-6} s^{-1}. After the specimen was broken, the fracture was ultrasonically cleaned for 10 min in acetone and absolute ethanol solutions and dried and sealed for SEM observation.

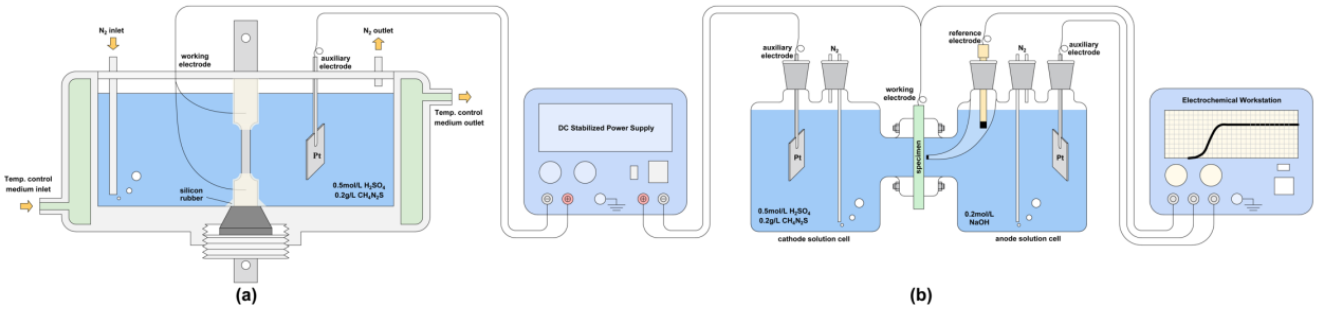


Figure 3. Schematic diagram of the device: (**a**) in situ hydrogen charging tensile, (**b**) D-S double electrolytic cell for hydrogen permeation.

Hydrogen permeation experiments [38,39] were carried out using the D-S double electrolytic cell shown in Figure 3b. The working electrode and the auxiliary electrode on the cathode side were connected to a DC stable power supply. The working electrode on the anode side, the auxiliary electrode, and the saturated calomel reference electrode constituted a three-electrode system connected to an electrochemical workstation. The electrochemical workstation recorded the hydrogen permeation current density change with time. The hydrogen permeation test temperature was 20 °C.

2.4. Characterization of the Fracture Surface

The fractured section was cut from the specimen using wire cutting, ultrasonically cleaned with acetone and anhydrous ethanol, and dried with cold air. The fracture surface was observed using a Hitachi S4800 cold field emission SEM (Hitachi, Tokyo, Japan).

3. Results and Discussion

3.1. Effect of Heat Input on Tensile Properties

To analyze the effect of heat input on the tensile properties of CGHAZ, engineering stress–strain curves of BM and CGHAZ without hydrogen were measured, as shown in Figure 4. The mechanical performance parameters were measured, and the results are shown in Table 2. The tensile curve of BM had an obvious yield point, while CGHAZ had no obvious yield point. As the heat input increased, the material's ultimate tensile strength (*UTS*) gradually decreased, but there was a slight increase for HI29.2. Simultaneously, the elongation (*EL*) of the material decreased with the increase in heat input, indicating that the higher the tensile strength, the worse the tensile toughness. When the heat input was $\leq$29.2 kJ/cm, the *UTS* of CGHAZ was significantly higher than BM. When the heat input was increased to 38.3 kJ/cm, the mechanical properties of CGHAZ were similar to BM. When the heat input continued to increase to 48.5 kJ/cm, the strength of CGHAZ was lower than that of BM, but the *EL* was higher than that of BM, showing a more substantial tensile toughness. The reduction in area (*RA*) in the CGHAZ was smaller than that of the BM.

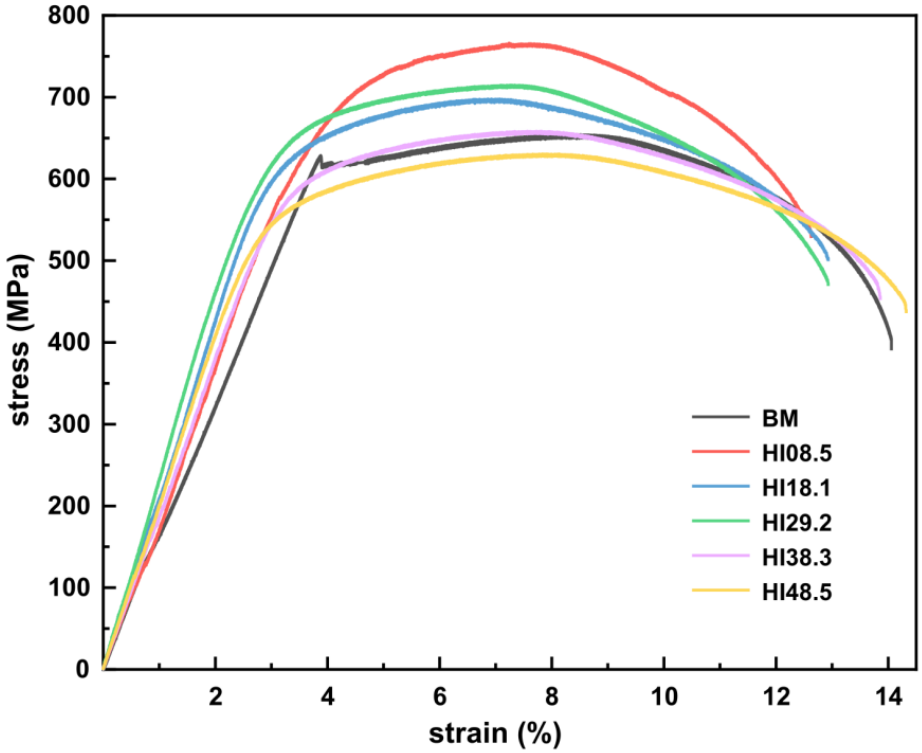


Figure 4. Stress–strain curve of BM and CGHAZ under different heat inputs.

Table 2. Tensile parameters of BM and CGHAZ under different heat inputs.

Label	*UTS* (MPa)	*RA* (%)	*EL* (%)
BM	654.28	36.61	14.06
HI08.5	766.21	25.70	12.65
HI18.1	697.95	25.87	13.14
HI29.2	714.97	26.56	13.25
HI38.3	658.58	28.20	14.05
HI48.5	630.68	28.76	14.48

3.2. Tensile Properties of CGHAZ with Different Heat Inputs at Different Hydrogen Concentrations

Slow tensile tests were performed on BM and CGHAZ under different heat inputs and hydrogen concentrations (including no hydrogen). The engineering stress–strain curves are shown in Figure 5. For BM, in the elastic stretching stage, the slope of the stress–strain curve increased obviously with the increase in hydrogen charging current density. Furthermore, the Young's modulus of the material gradually increased, and the stiffness of the material gradually increased. Nevertheless, for CGHAZ, in the elastic stretching stage, the Young's modulus of the material was less affected by hydrogen. In the presence of hydrogen atoms, whether BM or CGHAZ, the tensile specimens broke rapidly in the elastic stage. Hydrogen reduced the tensile properties of the materials, but there were apparent differences in the hydrogen embrittlement susceptibility among the different materials.

To clarify the effect of hydrogen on the tensile properties of the materials, we should pay attention to the concentration of hydrogen atoms rather than the hydrogen charging current density. Therefore, we used electrochemical hydrogen permeation experiments to determine the concentration of hydrogen atoms in the different materials at different hydrogen-charging current densities [40–43]. The hydrogen permeation curves of the materials with different heat inputs at different hydrogen charging current densities are shown in Figure 6.

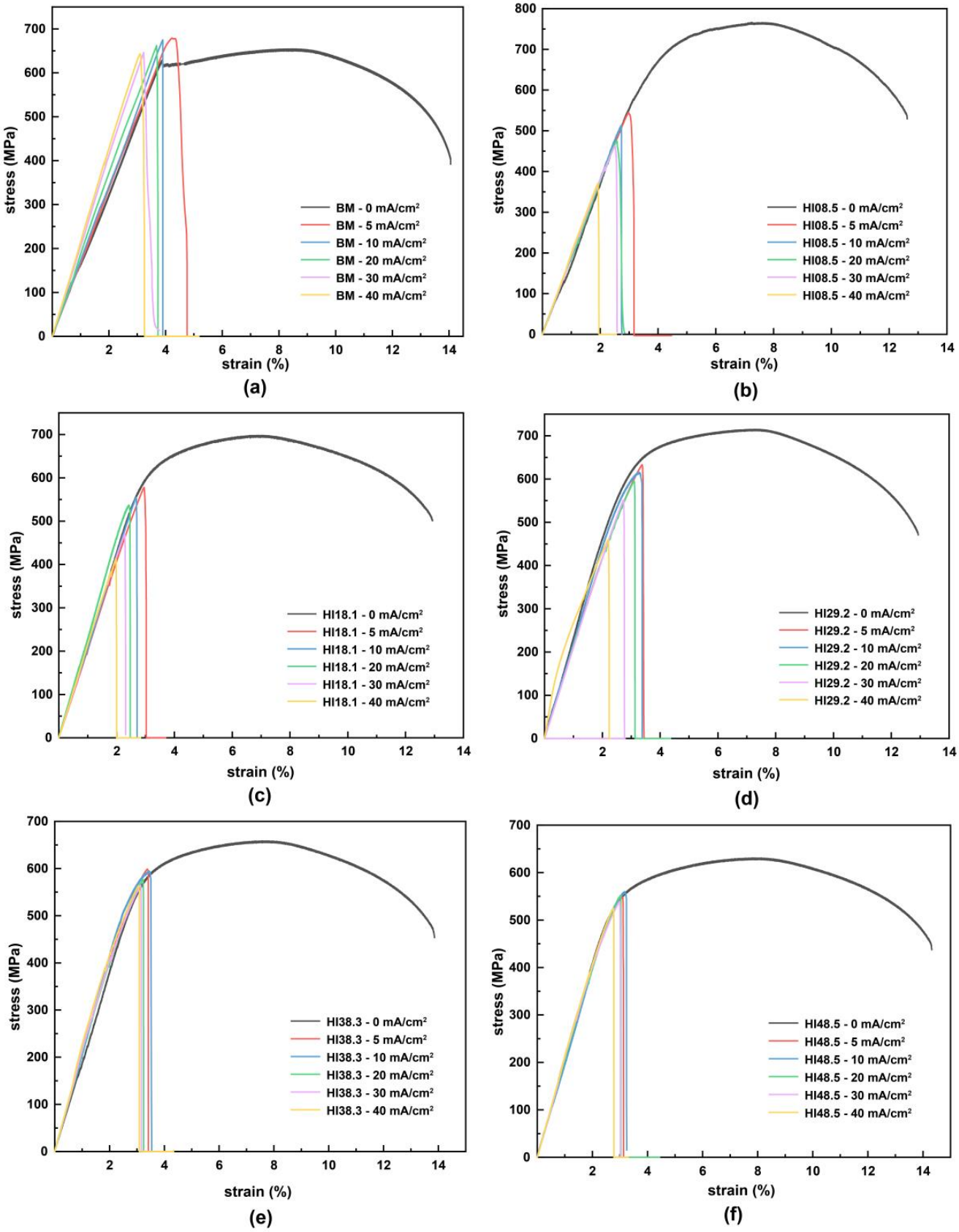


Figure 5. Stress–strain curves of materials with different heat inputs at different hydrogen charging current densities: (**a**) BM, (**b**) HI08.5, (**c**) HI18.1, (**d**) HI29.2, (**e**) HI38.3, (**f**) HI48.5.

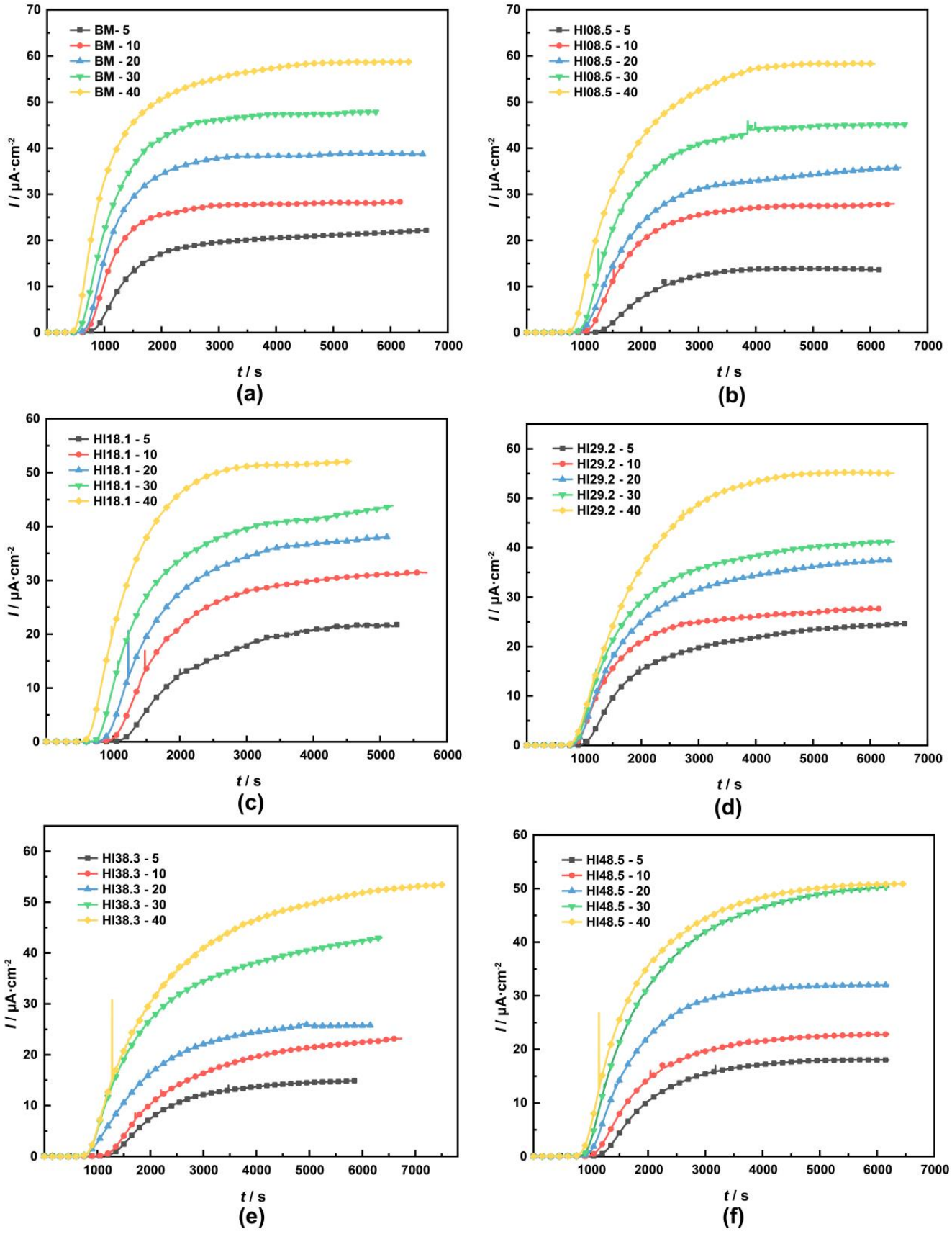


Figure 6. Hydrogen permeation curves of materials with different heat inputs at different hydrogen charging current densities: (**a**) BM, (**b**) HI08.5, (**c**) HI18.1, (**d**) HI29.2, (**e**) HI38.3, (**f**) HI48.5 [34].

The constant concentration (CC) model was chosen as the hydrogen permeation model [44–46]. For the CC model, the theoretical seepage transient current follows the dimensionless Formula (1):

$$\frac{I_t}{I\infty} = \frac{2}{\sqrt{\pi\tau}} \sum_{n=0}^{\infty} \exp\left(-\frac{(2n+1)^2}{4\tau}\right) \quad (1)$$

where I_t is the transient current density at time t; I_∞ is the steady-state current density; $\tau = Dt/L^2$ is a dimensionless parameter; D is the hydrogen diffusivity; and L is the thickness of the specimen.

The hydrogen diffusion coefficient D in this experiment was calculated using the Laplace method [47–49]. Moreover, the hydrogen concentration C_0 was calculated using the following formula:

$$C_0 = \frac{I_\infty L}{DF} \quad (2)$$

where F is the Faraday constant, and its value is 96,485 C/mol. The calculation results are shown in Table 3.

Table 3. Calculation results of hydrogen concentration for different heat input specimens at different hydrogen charging current densities.

Label	D (10^{-6} cm^2·s^{-1}) C_0 (10^{-5} mol·cm^{-3})									
	I = 5 mA/cm^2		I = 10 mA/cm^2		I = 20 mA/cm^2		I = 30 mA/cm^2		I = 40 mA/cm^2	
	D	C_0	D	C_0	D	C_0	D	C_0	D	C_0
BM	3.978	1.123	4.932	1.131	4.863	1.606	4.991	1.914	5.304	2.227
HI08.5	3.123	0.928	3.025	1.72	3.454	2.144	3.687	2.554	3.834	3.115
HI18.1	2.725	1.626	3.248	1.911	3.586	2.113	4.043	2.162	4.881	2.177
HI29.2	3.287	1.553	3.348	1.699	3.440	2.252	3.641	2.323	3.953	2.897
HI38.3	2.477	1.236	2.755	1.725	3.010	1.757	3.100	2.847	3.247	3.411
HI48.5	3.079	1.203	3.152	1.474	3.157	2.080	3.447	2.995	3.521	3.036

The *UTS* and *EL* were obtained according to the stress–strain curve in Figure 5. *RA* was obtained from fracture dimension measurements. Measurements were taken at three locations of the fracture surface, to obtain an average value. According to the hydrogen concentrations of the different heat input specimens at different hydrogen charging current densities in Table 3, the hydrogen charging current density was replaced by the hydrogen concentration. The *UTS*, *EL*, and *RA* under different hydrogen charging current densities, hydrogen concentrations, and HI were obtained, as shown in Figures 7–9. As depicted in Figure 7c, it can be observed that a minor welding heat input led to an improvement in the *UTS*, with HI08.5 exhibiting the highest *UTS* value under a tension load. However, when hydrogen atoms were present, as shown in Figure 7b, the *UTS* of the CGHAZ gradually decreased with the increase in hydrogen concentration, and the smaller the heat input, the more significant the decrease in *UTS*. For this scenario, the *UTS* of HI08.5 and HI18.1 was the worst.

In the absence of hydrogen atoms, the CGHAZ achieved desirable elongation characteristics, with *EL* gradually increasing with the increase in welding heat input. Notably, at HI48.5, the elongation rate reached 14.48%, surpassing BM. Figure 8c shows that the elongation rate dropped significantly once the hydrogen atoms entered the material. From Figure 8d,b, with the increase in the hydrogen charging current density, the elongation of the material decreased. The *UTS* of HI08.5 and HI18.1 was the worst. *EL* refers to the ability of a material to deform when stretched. The greater the elongation, the better the toughness of the material. Hydrogen atoms can cause a material to lose its toughness rapidly, especially when the material microstructure has a substantial content of LB.

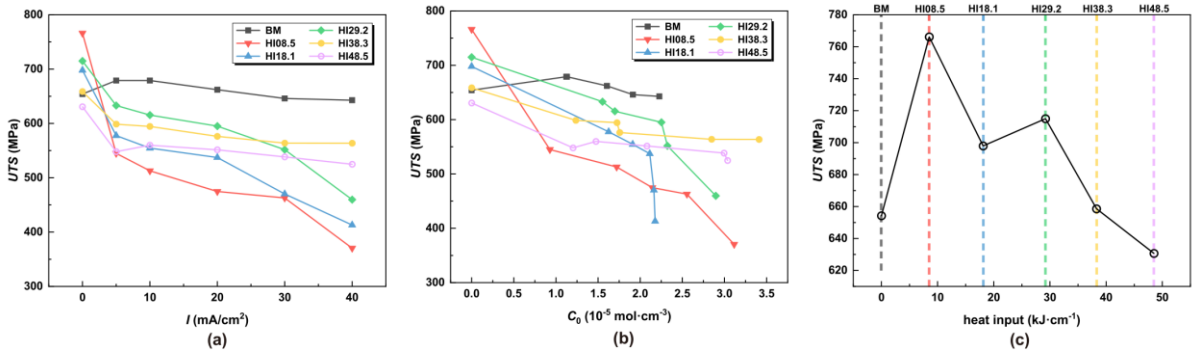


Figure 7. *UTS* at different hydrogen charging current densities, hydrogen concentrations, and HI (**a**) under different *I*, (**b**) under different C_0, and (**c**) under different HI.

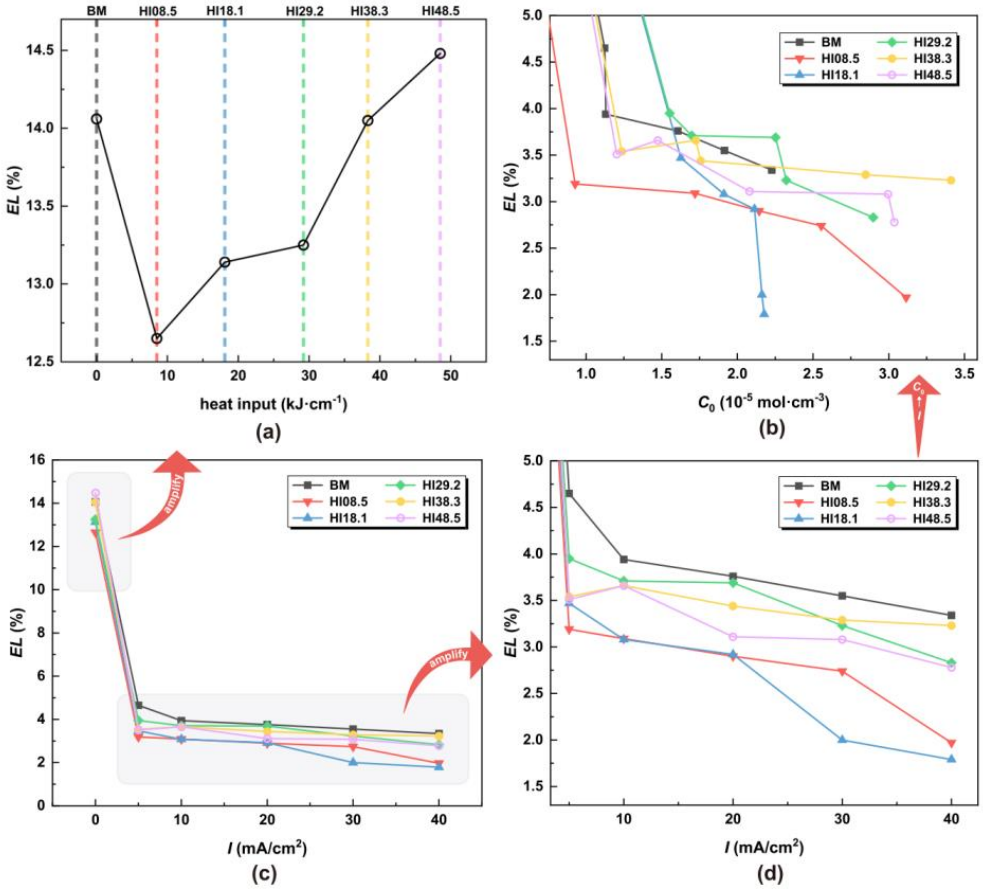


Figure 8. *EL* under different HI, hydrogen charging current density, and hydrogen concentration (**a**) under different HI, (**b**) under different C_0, (**c**) under different *I*, and (**d**) local amplification under different *I*.

As shown in Figure 9a, in the absence of hydrogen atoms, the *RA* of CGHAZ was lower than that of the BM. For CGHAZ, with the increase in HI, *RA* gradually increased, indicating that the plasticity of the material was enhanced. As shown in Figure 9c, the *RA* dropped significantly once the material came into contact with hydrogen atoms. From Figure 9d,b, with the increase in hydrogen concentration, the *RA* of the material decreased gradually, indicating a loss of plasticity of the material. The *EL* and *RA* of HI18.1 showed a continuous and sharp drop around the hydrogen concentrations of 1.5×10^{-5} mol·cm^{-3} and 2.2×10^{-5} mol·cm^{-3}. This proves that the plasticity of the material dropped sharply.

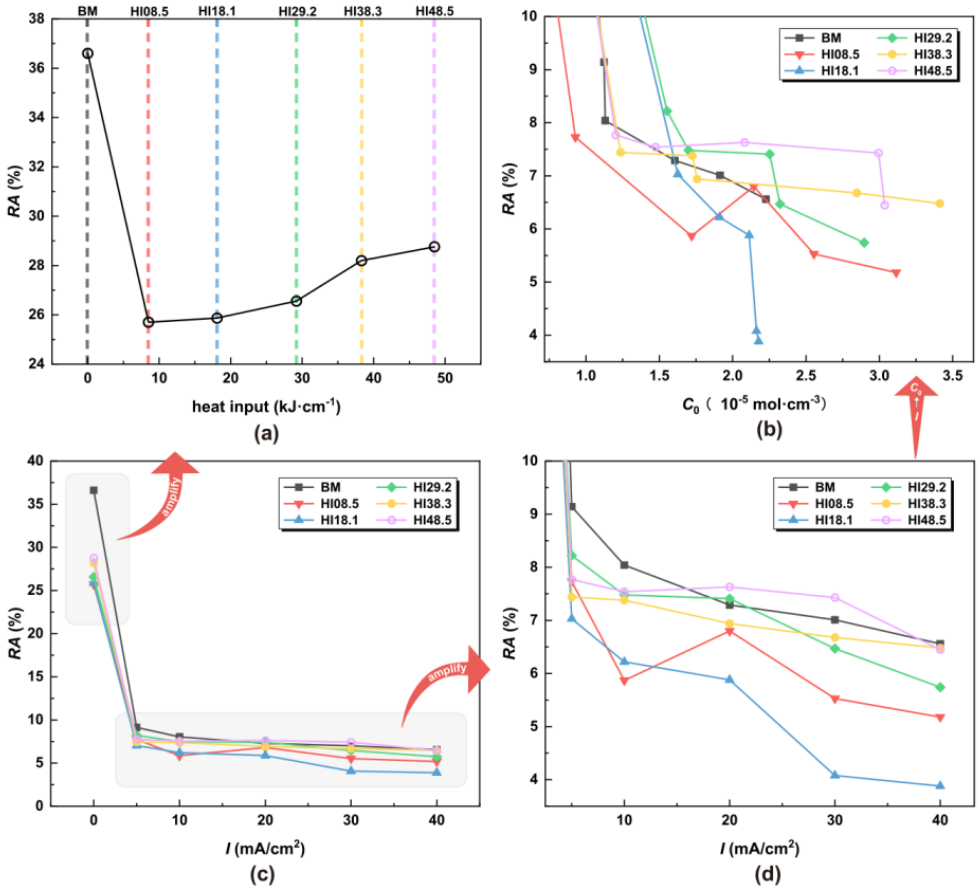


Figure 9. *RA* under different HI, hydrogen charging current densities, and hydrogen concentrations: (**a**) under different HI, (**b**) under different C_0, (**c**) under different I, and (**d**) local amplification under different I.

The relative elongation ΔEL was used to characterize the hydrogen embrittlement susceptibility of the material, and its expression is

$$\Delta EL = \frac{EL_{w/oH} - EL_{withH}}{EL_{w/oH}} \times 100\% \quad (3)$$

where $EL_{w/oH}$ is the elongation without hydrogen, and EL_{withH} is the elongation with hydrogen. The ΔEL of CGHAZ with different heat inputs at different hydrogen concentrations was calculated, respectively. The calculation results are shown in Figure 10.

When the heat input was set to 29.2 kJ/cm, CGHAZ had the lowest hydrogen embrittlement sensitivity under tensile load, even lower than the BM. When HI > 29.2 kJ/cm, the susceptibility to hydrogen embrittlement of CGHAZ was less affected by the hydrogen concentration gradient. At this stage, the susceptibility to hydrogen embrittlement was slightly higher than that of BM, steadily increasing with an escalating hydrogen concentration. When HI <29.2 kJ/cm, the hydrogen embrittlement susceptibility of HI18.1 was the highest, and the susceptibility to hydrogen embrittlement increased rapidly with the increase in the hydrogen concentration. The welding heat input associated with HI18.1 precisely matched the welding parameter used in the current operational pipeline.

3.3. Fracture Surface Analysis of CGHAZ with Different Heat Inputs

The tensile fracture surfaces of the CGHAZ specimens under different heat inputs without hydrogen charging and at a hydrogen charging current density of 20 mA/cm^2 are shown in Figure 11.

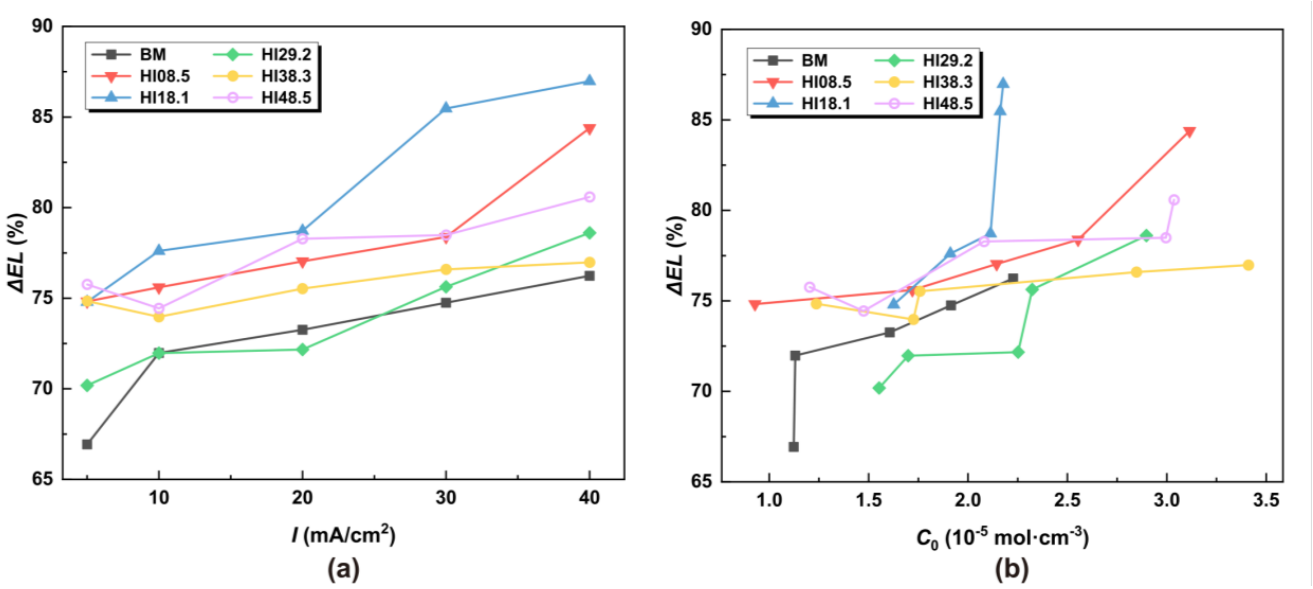


Figure 10. Δ*EL* under different hydrogen charging current densities and hydrogen concentrations: (**a**) under different *I*, (**b**) under different C_0.

Without hydrogen, the tensile fracture surfaces under different heat inputs were characterized by ductile fracture. Dimple structures dominated the fracture surface, and dense small dimples were distributed around large ones. Furthermore, there was an apparent necking phenomenon. With the increase in heat input, the area and content of large dimples in the fracture surface increased, indicating that the material's toughness had increased. When it reached HI29.2, small cracks and inclusion holes appeared on the fracture surface. In the presence of hydrogen, the fracture surface showed brittle fracture characteristics. HI08.5 exhibited intergranular fractures, and deep cracks were observed on the fracture surface. The hydrogen accumulated in the specimen reduced the critical stress of crack initiation and had a specific auxiliary effect on crack propagation [50–52]. Therefore, the large cracks propagated in different directions, leading to the rapid fracturing of the specimen under hydrogen charging. At HI18.1, intergranular and transgranular fractures existed in the fracture surface, and a clear boundary between them could be observed. At HI29.2, the fracture surface mainly showed a transgranular fracture, but there were apparent tearing edges on the fracture surface. The surface of the transgranular fracture was truncated at multiple points, and there were apparent step structures between the river-like patterns. The fracture surfaces resulting from HI38.3 and HI48.5 exhibited transgranular brittle fractures, with the surfaces becoming progressively flatter. The step area of the river-like pattern also gradually increased, and the secondary cracks gradually became more extensive and deeper.

3.4. Mechanism of the Difference in Sensitivity of LB and GB to HIC under a Tensile Load

HIC analysis was performed of the metallographic structure of CGHAZ with different heat inputs and of its tensile properties under different hydrogen concentrations. In the absence of hydrogen, the bulk LB enhanced the tensile strength of CGHAZ and improved the material performance [53,54]. Nevertheless, when hydrogen was present, the bulk LB exhibited a high sensitivity to hydrogen embrittlement, and the materials predominantly composed of bulk LB demonstrated a weak resistance to hydrogen embrittlement. In the presence of hydrogen, the composite structure of fine LB and GB had the best resistance to hydrogen embrittlement. The susceptibility to hydrogen embrittlement of the pure GB structure was less affected by changes in the hydrogen concentration. The mechanism of the influence of LB and GB on HIC under tensile load was analyzed, as shown in Figure 12. Hydrogen atoms tended to accumulate in the grain boundaries [55]. When the

hydrogen atoms gathered in the bulk LB grain boundaries, the grain boundaries of long strips tended to initiate intergranular cracks under a tensile load, as shown in Figure 12a. When the microstructure became a composite microstructure of fine LB and GB, as shown in Figure 12b, the extended grain boundaries in the original bulk LB were divided by GB. Segmentation made the intergranular cracks more likely to be blocked, so the fracture surface presented mixed intergranular and transgranular fractures. The fracture was transgranular when the metallographic structure became pure GB, as shown in Figure 12c. Hydrogen atoms only acted on cracks passing through the grain boundaries, so their susceptibility to hydrogen embrittlement was less affected by changes in the hydrogen concentration. Therefore, under a tension load, the fine LB and GB composite structure in Figure 12b shows a better resistance to hydrogen embrittlement. This is a more desirable structure in metal metallurgy and welding processes.

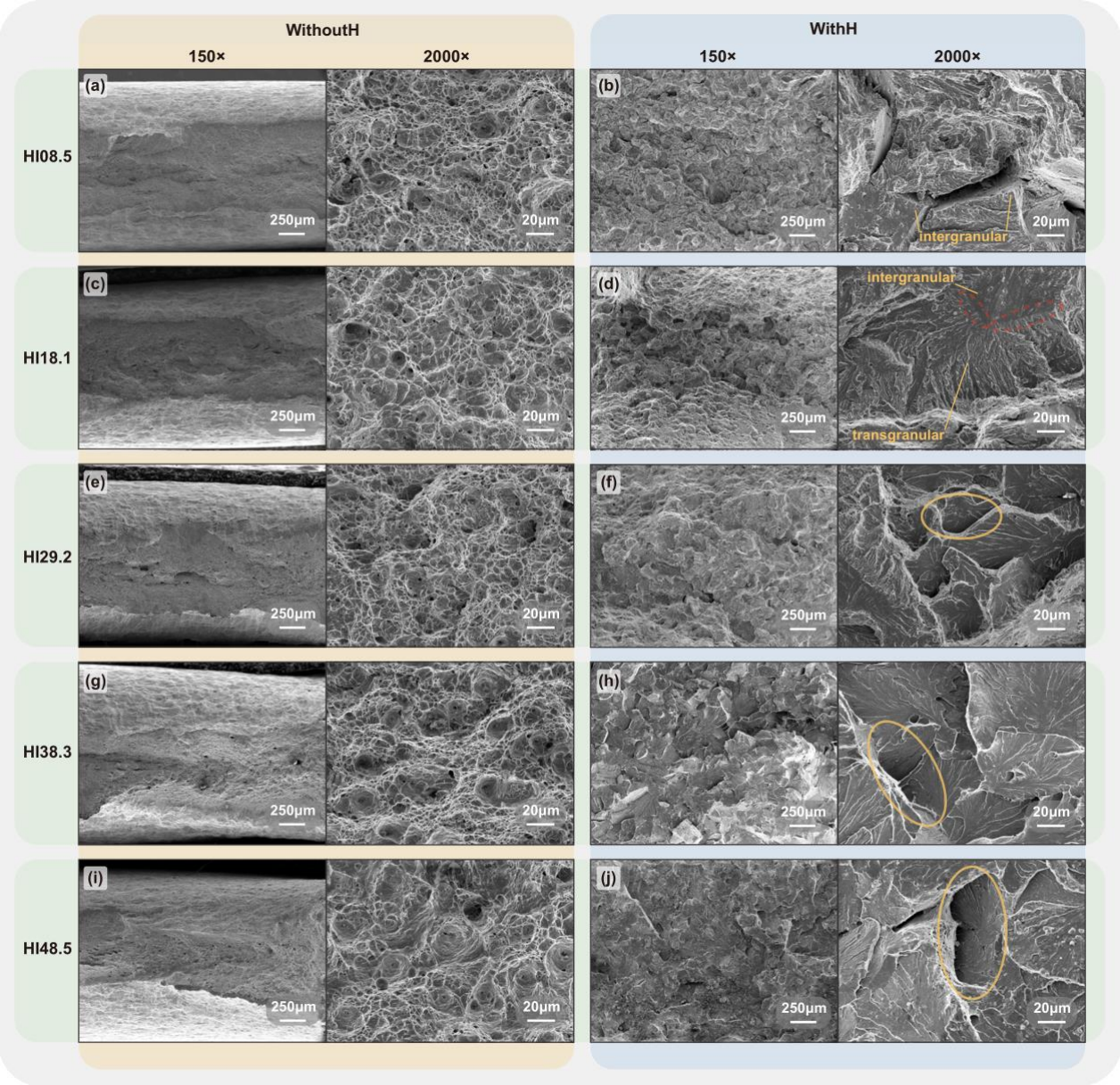


Figure 11. Fracture surface of X80 Steel CGHAZ: without hydrogen—(**a**) HI08.5, (**c**) HI18.1, (**e**) HI29.2, (**g**) HI38.3, (**i**) HI48.5; with hydrogen—(**b**) HI08.5, (**d**) HI18.1, (**f**) HI29.2, (**h**) HI38.3, (**j**) HI48.5.

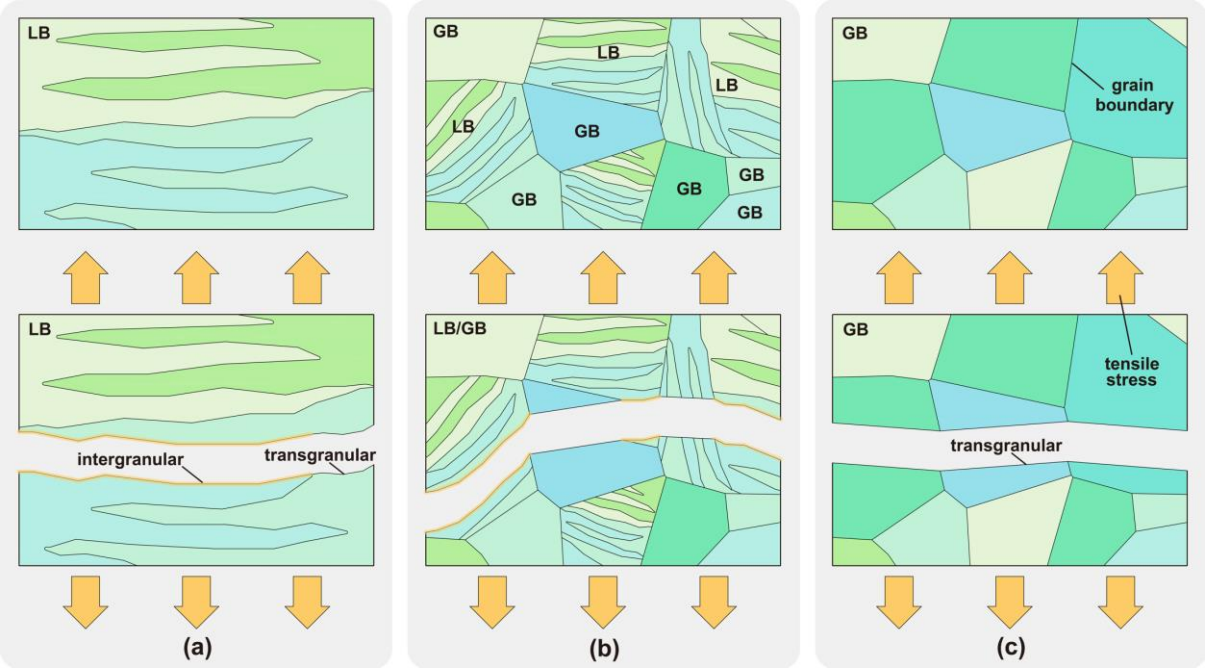


Figure 12. HIC of LB and GB under tension load: (**a**) LB, (**b**) LB and GB, (**c**) GB.

According to the microstructure content and the arresting effect of the different structures on HIC, a comparison of HIC resistance of the different microstructures is summarized in Table 4. This verifies that 11% LB steel had a better HE resistance. Moreover, these LBs should be scattered in GB.

Table 4. Comparison of the microstructure and HIC resistance of CGHAZ.

Label	LB and GB Content	Microstructure Distribution	Fracture Characteristics with Hydrogen	HE Resistance
HI08.5	LB: 88.0% GB: 8.5%	mainly LB, finely intertwined	intergranular fracture	high susceptibility to HE
HI18.1	LB: 70.5% GB: 26.8%		intergranular and transgranular mixed fracture	
HI29.2	LB: 11.0% GB: 82.4%	LB mixed with GB, LB dispersed in GB	transgranular fracture with stepped truncation	minimal susceptibility to HE
HI38.3	LB: 1.7% GB: 94.1%	mainly GB	flat transcrystalline fracture	less affected by hydrogen concentration
HI48.5	LB: 0.8% GB: 95.5%			

4. Conclusions

1. An increment in hydrogen concentration resulted in an increased Young's modulus of BM during the elastic stretching stage. However, this effect was not prominent in CGHAZ. The *UTS* of CGHAZ gradually decreased with the increase in hydrogen concentration. Once the material was exposed to hydrogen, the material plasticity dropped sharply at first and then decreased slowly with the increased hydrogen concentration.
2. The HI 29.2 specimen had the lowest sensitivity to HE under tensile load. The HE sensitivity of HI38.3 and HI48.5 became less affected by the hydrogen concentration gradient. The HE susceptibility of HI18.1 was the highest, and its HE susceptibility increased rapidly with the hydrogen concentration.

3. In the presence of hydrogen, the fracture surface showed brittle fracture characteristics. HI08.5 demonstrated intergranular fracture behavior. HI18.1 showed mixed transgranular and intergranular fractures. For HI29.2, the fracture surface mainly showed a transgranular fracture with stepped truncation. For HI38.3 and HI48.5, the fracture surfaces exhibited transgranular brittle fracture, with the surfaces becoming progressively flatter.
4. Steels predominantly composed of bulk LB were vulnerable to hydrogen embrittlement and exhibit intergranular cracking. A fine LB and GB composite structure can remarkably obstruct intergranular cracks, giving a superior resistance to hydrogen embrittlement. The LB content of hydrogen-resistant steels is expected to be about 11%, and LB should be scattered in GB.

Author Contributions: Conceptualization, J.G. and G.C.; Data curation, J.G. and X.D.; Funding acquisition, X.X. and Z.L.; Methodology, J.G. and J.L.; Resources, X.X. and Z.L.; Supervision, J.L.; Writing—original draft, J.G. and X.D.; Writing—review and editing, J.G., X.X., G.C., Z.L. and J.L. All authors have read and agreed to the published version of the manuscript.

Funding: This research was funded by the Natural Science Foundation of Shandong Province [ZR2020ME094], National Natural Science Foundation of China [52004323], Senior Foreign Expert Project Foundation [G2022152003L], and CNPC Innovation Foundation [2022DQ02-0502].

Data Availability Statement: The data supporting this study's findings are available from the corresponding author upon reasonable request.

Conflicts of Interest: The authors declare that they have no known competing financial interest or personal relationships that could have appeared to influence the work reported in this paper.

References

1. Koohi-Fayegh, S.; Rosen, M.A. A Review of Energy Storage Types, Applications and Recent Developments. *J. Energy Storage* **2020**, *27*, 101047. [CrossRef]
2. Smith, C.; Hill, A.K.; Torrente-Murciano, L. Current and Future Role of Haber–Bosch Ammonia in a Carbon-Free Energy Landscape. *Energy Environ. Sci.* **2020**, *13*, 331–344. [CrossRef]
3. Abdin, Z.; Zafaranloo, A.; Rafiee, A.; Mérida, W.; Lipiński, W.; Khalilpour, K.R. Hydrogen as an Energy Vector. *Renew. Sustain. Energy Rev.* **2020**, *120*, 109620. [CrossRef]
4. Dawood, F.; Anda, M.; Shafiullah, G.M. Hydrogen Production for Energy: An Overview. *Int. J. Hydrogen Energy* **2020**, *45*, 3847–3869. [CrossRef]
5. Messaoudani, Z.L.; Rigas, F.; Binti Hamid, M.D.; Che Hassan, C.R. Hazards, Safety and Knowledge Gaps on Hydrogen Transmission via Natural Gas Grid: A Critical Review. *Int. J. Hydrogen Energy* **2016**, *41*, 17511–17525. [CrossRef]
6. Jaworski, J.; Kułaga, P.; Blacharski, T. Study of the Effect of Addition of Hydrogen to Natural Gas on Diaphragm Gas Meters. *Energies* **2020**, *13*, 3006. [CrossRef]
7. Zhang, P.; Laleh, M.; Hughes, A.E.; Marceau, R.K.W.; Hilditch, T.; Tan, M.Y. A Systematic Study on the Influence of Electrochemical Charging Conditions on the Hydrogen Embrittlement Behaviour of a Pipeline Steel. *Int. J. Hydrogen Energy* **2023**, *48*, 16501–16516. [CrossRef]
8. Zhang, L.; Shen, H.; Lu, K.; Cao, W.; Sun, Y.; Fang, Y.; Xing, Y.; Du, Y.; Lu, M. Investigation of Hydrogen Concentration and Hydrogen Damage on API X80 Steel Surface under Cathodic Overprotection. *Int. J. Hydrogen Energy* **2017**, *42*, 29888–29896. [CrossRef]
9. Singh, V.; Singh, R.; Arora, K.S.; Mahajan, D.K. Hydrogen Induced Blister Cracking and Mechanical Failure in X65 Pipeline Steels. *Int. J. Hydrogen Energy* **2019**, *44*, 22039–22049. [CrossRef]
10. Sanchez, L.; Cong, H. AC Interference on Hydrogen Absorption in Low Carbon Steel under Cathodic Protection. *Int. J. Hydrogen Energy* **2023**, *48*, 1202–1217. [CrossRef]
11. Zhang, T.; Zhao, W.; Li, T.; Zhao, Y.; Deng, Q.; Wang, Y.; Jiang, W. Comparison of Hydrogen Embrittlement Susceptibility of Three Cathodic Protected Subsea Pipeline Steels from a Point of View of Hydrogen Permeation. *Corros. Sci.* **2018**, *131*, 104–115. [CrossRef]
12. An, T.; Zhang, S.; Feng, M.; Luo, B.; Zheng, S.; Chen, L.; Zhang, L. Synergistic Action of Hydrogen Gas and Weld Defects on Fracture Toughness of X80 Pipeline Steel. *Int. J. Fatigue* **2019**, *120*, 23–32. [CrossRef]
13. Zhou, D.; Li, T.; Huang, D.; Wu, Y.; Huang, Z.; Xiao, W.; Wang, Q.; Wang, X. The Experiment Study to Assess the Impact of Hydrogen Blended Natural Gas on the Tensile Properties and Damage Mechanism of X80 Pipeline Steel. *Int. J. Hydrogen Energy* **2021**, *46*, 7402–7414. [CrossRef]

14. Li, X.; Ma, X.; Zhang, J.; Akiyama, E.; Wang, Y.; Song, X. Review of Hydrogen Embrittlement in Metals: Hydrogen Diffusion, Hydrogen Characterization, Hydrogen Embrittlement Mechanism and Prevention. *Acta Metall. Sin. (Engl. Lett.)* **2020**, *33*, 759–773. [CrossRef]
15. Zhao, H.; Chakraborty, P.; Ponge, D.; Hickel, T.; Sun, B.; Wu, C.-H.; Gault, B.; Raabe, D. Hydrogen Trapping and Embrittlement in High-Strength Al Alloys. *Nature* **2022**, *602*, 437–441. [CrossRef] [PubMed]
16. Liu, Q.; Venezuela, J.; Zhang, M.; Zhou, Q.; Atrens, A. Hydrogen Trapping in Some Advanced High Strength Steels. *Corros. Sci.* **2016**, *111*, 770–785. [CrossRef]
17. Sun, Y.; Cheng, Y.F. Hydrogen Permeation and Distribution at a High-Strength X80 Steel Weld under Stressing Conditions and the Implication on Pipeline Failure. *Int. J. Hydrogen Energy* **2021**, *46*, 23100–23112. [CrossRef]
18. Sun, Y.; Cheng, Y.F. Thermodynamics of Spontaneous Dissociation and Dissociative Adsorption of Hydrogen Molecules and Hydrogen Atom Adsorption and Absorption on Steel under Pipelining Conditions. *Int. J. Hydrogen Energy* **2021**, *46*, 34469–34486. [CrossRef]
19. Köse, C. Effect of Heat Input and Post Weld Heat Treatment on the Texture, Microstructure and Mechanical Properties of Laser Beam Welded AISI 317L Austenitic Stainless Steel. *Mater. Sci. Eng. A* **2022**, *855*, 143966. [CrossRef]
20. Köse, C. Heat Treatment and Heat Input Effects on the Dissimilar Laser Beam Welded AISI 904L Super Austenitic Stainless Steel to AISI 317L Austenitic Stainless Steel: Surface, Texture, Microstructure and Mechanical Properties. *Vacuum* **2022**, *205*, 111440. [CrossRef]
21. Köse, C.; Topal, C. Texture, Microstructure and Mechanical Properties of Laser Beam Welded AISI 2507 Super Duplex Stainless Steel. *Mater. Chem. Phys.* **2022**, *289*, 126490. [CrossRef]
22. Panin, S.V.; Maruschak, P.O.; Vlasov, I.V.; Syromyatnikova, A.S.; Bolshakov, A.M.; Berto, F.; Prentkovskis, O.; Ovechkin, B.B. Effect of Operating Degradation in Arctic Conditions on Physical and Mechanical Properties of 09Mn2Si Pipeline Steel. *Procedia Eng.* **2017**, *178*, 597–603. [CrossRef]
23. Yang, Y.; Shi, L.; Xu, Z.; Lu, H.; Chen, X.; Wang, X. Fracture Toughness of the Materials in Welded Joint of X80 Pipeline Steel. *Eng. Fract. Mech.* **2015**, *148*, 337–349. [CrossRef]
24. Li, R.; Zuo, X.; Hu, Y.; Wang, Z.; Hu, D. Microstructure and Properties of Pipeline Steel with a Ferrite/Martensite Dual-Phase Microstructure. *Mater. Charact.* **2011**, *62*, 801–806. [CrossRef]
25. Li, J.; Li, H.; Peng, W.; Xiang, T.; Xu, Z.; Yang, J. Effect of Simulated Welding Thermal Cycles on Microstructure and Mechanical Properties of Coarse-Grain Heat-Affected Zone of High Nitrogen Austenitic Stainless Steel. *Mater. Charact.* **2019**, *149*, 206–217. [CrossRef]
26. Sun, Y.; Fujii, H.; Imai, H.; Kondoh, K. Suppression of Hydrogen-Induced Damage in Friction Stir Welded Low Carbon Steel Joints. *Corros. Sci.* **2015**, *94*, 88–98. [CrossRef]
27. Duan, R.H.; Wang, Y.Q.; Luo, Z.A.; Wang, G.D.; Xie, G.M. Hydrogen Embrittlement Behavior in the Nugget Zone of Friction Stir Welded X100 Pipeline Steel. *Int. J. Hydrogen Energy* **2023**, *48*, 8296–8309. [CrossRef]
28. Zhao, W.; Zhang, T.; Zhao, Y.; Sun, J.; Wang, Y. Hydrogen Permeation and Embrittlement Susceptibility of X80 Welded Joint under High-Pressure Coal Gas Environment. *Corros. Sci.* **2016**, *111*, 84–97. [CrossRef]
29. Zhang, T.; Zhao, W.; Deng, Q.; Jiang, W.; Wang, Y.; Wang, Y.; Jiang, W. Effect of Microstructure Inhomogeneity on Hydrogen Embrittlement Susceptibility of X80 Welding HAZ under Pressurized Gaseous Hydrogen. *Int. J. Hydrogen Energy* **2017**, *42*, 25102–25113. [CrossRef]
30. Deng, Q.; Zhao, W.; Jiang, W.; Zhang, T.; Li, T.; Zhao, Y. Hydrogen Embrittlement Susceptibility and Safety Control of Reheated CGHAZ in X80 Welded Pipeline. *J. Mater. Eng. Perform.* **2018**, *27*, 1654–1663. [CrossRef]
31. Zhang, Y.; Liu, N.; Li, Z.; Zhang, G.; Yuan, H.; Xu, W.; Gao, Z.; Mi, J. Gleeble Experiments Concerning Dendrite Re-Melting and Its Role in Microstructural Evolution in Spray Formed High-Alloy Metals. *Rare Met.* **2011**, *30*, 401–404. [CrossRef]
32. Sirin, K.; Sirin, S.Y.; Kaluc, E. Influence of the Interpass Temperature on T8/5 and the Mechanical Properties of Submerged Arc Welded Pipe. *J. Mater. Process. Technol.* **2016**, *238*, 152–159. [CrossRef]
33. Xu, W.W.; Wang, Q.F.; Pan, T.; Su, H.; Yang, C.F. Effect of Welding Heat Input on Simulated HAZ Microstructure and Toughness of a V-N Microalloyed Steel. *J. Iron Steel Res. Int.* **2007**, *14*, 234–239. [CrossRef]
34. Gou, J.; Nie, R.; Xing, X.; Li, Z.; Cui, G.; Liu, J.; Deng, X.; Cheng, Y.F. Hydrogen-Induced Cracking of Welded X80 Steel Studies by Experimental Testing and Molecular Dynamics Modeling. *Corros. Sci.* **2023**, *214*, 111027. [CrossRef]
35. Huda, N.; Midawi, A.; Gianetto, J.A.; Gerlich, A.P. Continuous Cooling Transformation Behaviour and Toughness of Heat-Affected Zones in an X80 Line Pipe Steel. *J. Mater. Res. Technol.* **2021**, *12*, 613–628. [CrossRef]
36. Xing, X.; Cheng, R.; Cui, G.; Liu, J.; Gou, J.; Yang, C.; Li, Z.; Yang, F. Quantification of the Temperature Threshold of Hydrogen Embrittlement in X90 Pipeline Steel. *Mater. Sci. Eng. A* **2021**, *800*, 140118. [CrossRef]
37. Li, X.; Wang, Y.; Zhang, P.; Li, B.; Song, X.; Chen, J. Effect of Pre-Strain on Hydrogen Embrittlement of High Strength Steels. *Mater. Sci. Eng. A* **2014**, *616*, 116–122. [CrossRef]
38. Gou, J.; Deng, X.; Cui, G.; Xing, X.; Li, Z. Research on Hydrogen Permeation in the X80 Steel Heat-Affected Zone with Different Heat Inputs. *J. Phys. Conf. Ser.* **2022**, *2383*, 012140. [CrossRef]
39. Koren, E.; Hagen, C.M.; Wang, D.; Lu, X.; Johnsen, R.; Yamabe, J. Experimental Comparison of Gaseous and Electrochemical Hydrogen Charging in X65 Pipeline Steel Using the Permeation Technique. *Corros. Sci.* **2023**, *215*, 111025. [CrossRef]

40. Van den Eeckhout, E.; Verbeken, K.; Depover, T. Methodology of the Electrochemical Hydrogen Permeation Test: A Parametric Evaluation. *Int. J. Hydrogen Energy* **2023**. [CrossRef]
41. Peral, L.B.; Amghouz, Z.; Colombo, C.; Fernández-Pariente, I. Evaluation of Hydrogen Trapping and Diffusion in Two Cold Worked CrMo(V) Steel Grades by Means of the Electrochemical Hydrogen Permeation Technique. *Theor. Appl. Fract. Mech.* **2020**, *110*, 102771. [CrossRef]
42. Cheng, Y.F. Analysis of Electrochemical Hydrogen Permeation through X-65 Pipeline Steel and Its Implications on Pipeline Stress Corrosion Cracking. *Int. J. Hydrogen Energy* **2007**, *32*, 1269–1276. [CrossRef]
43. Addach, H.; Berçot, P.; Rezrazi, M.; Takadoum, J. Study of the Electrochemical Permeation of Hydrogen in Iron. *Corros. Sci.* **2009**, *51*, 263–267. [CrossRef]
44. Zhao, W.; Zhang, T.; He, Z.; Sun, J.; Wang, Y. Determination of the Critical Plastic Strain-Induced Stress of X80 Steel through an Electrochemical Hydrogen Permeation Method. *Electrochim. Acta* **2016**, *214*, 336–344. [CrossRef]
45. Xu, Z.; Zhang, P.; Meng, G.; Wang, Y.; Wang, J.; Shao, Y.; Wang, F. Influence of Low Tensile Stress on the Kinetics of Hydrogen Permeation and Evolution Behavior in Alkaline Environment. *Int. J. Hydrogen Energy* **2022**, *47*, 33803–33812. [CrossRef]
46. Díaz, A.; Zafra, A.; Martínez-Pañeda, E.; Alegre, J.M.; Belzunce, J.; Cuesta, I.I. Simulation of Hydrogen Permeation through Pure Iron for Trapping and Surface Phenomena Characterisation. *Theor. Appl. Fract. Mech.* **2020**, *110*, 102818. [CrossRef]
47. Jebaraj, J.J.M.; Morrison, D.J.; Suni, I.I. Hydrogen Diffusion Coefficients through Inconel 718 in Different Metallurgical Conditions. *Corros. Sci.* **2014**, *80*, 517–522. [CrossRef]
48. Meng, G.; Sun, F.; Wang, S.; Shao, Y.; Zhang, T.; Wang, F. Effect of Electrodeposition Parameters on the Hydrogen Permeation during Cu–Sn Alloy Electrodeposition. *Electrochim. Acta* **2010**, *55*, 2238–2245. [CrossRef]
49. Izadi, H.; Tavakoli, M.; Moayed, M.H. Effect of Thermomechanical Processing on Hydrogen Permeation in API X70 Pipeline Steel. *Mater. Chem. Phys.* **2018**, *220*, 360–365. [CrossRef]
50. Olden, V.; Alvaro, A.; Akselsen, O.M. Hydrogen Diffusion and Hydrogen Influenced Critical Stress Intensity in an API X70 Pipeline Steel Welded Joint-Experiments and FE Simulations. *Int. J. Hydrogen Energy* **2012**, *37*, 11474–11486. [CrossRef]
51. Kumai, B.; Hojo, T.; Koyama, M.; Akiyama, E.; Waki, H.; Nagasaka, A. Pre-Strain Effects on Critical Stress and Hydrogen Content for Hydrogen-Induced Quasi-Cleavage Fracture in a TRIP-Aided Bainitic Ferrite Steel: Martensitic Transformation, Matrix Damage, and Strain Aging. *Int. J. Hydrogen Energy* **2020**, *45*, 27920–27928. [CrossRef]
52. Sun, Y.; Frank Cheng, Y. Hydrogen-Induced Degradation of High-Strength Steel Pipeline Welds: A Critical Review. *Eng. Fail. Anal.* **2022**, *133*, 105985. [CrossRef]
53. Krauss, G.; Thompson, S.W. Ferritic Microstructures in Continuously Cooled Low- and Ultralow-Carbon Steels. *ISIJ Int.* **1995**, *35*, 937–945. [CrossRef]
54. Li, C.; Wang, Y.; Han, T.; Han, B.; Li, L. Microstructure and Toughness of Coarse Grain Heat-Affected Zone of Domestic X70 Pipeline Steel during in-Service Welding. *J. Mater. Sci.* **2011**, *46*, 727–733. [CrossRef]
55. Xing, X.; Gou, J.; Li, F.; Zhang, Y.; Cheng, J.; Wang, Y.; Liu, J.; Cui, G.; Li, Z.; Zhang, P.; et al. Hydrogen Effect on the Intergranular Failure in Polycrystal Ɑ-Iron with Different Crystal Sizes. *Int. J. Hydrogen Energy* **2021**, *46*, 36528–36538. [CrossRef]

Disclaimer/Publisher's Note: The statements, opinions and data contained in all publications are solely those of the individual author(s) and contributor(s) and not of MDPI and/or the editor(s). MDPI and/or the editor(s) disclaim responsibility for any injury to people or property resulting from any ideas, methods, instructions or products referred to in the content.